Active Phase Control to Enhance Distance Relay in Converter-Interfaced Renewable Energy Systems

Haobo Zhang, Wang Xiang, Qiteng Hong, Jinyu Wen

***Abstract*- For the distance protection applied in converter-interfaced renewable energy systems, various AC fault ride-through strategies of converter-interfaced sources will cause a large phase difference between the operating current of the distance relay and the fault current, resulting in the mal-operation of the distance relay. To overcome this issue, this paper proposes an active phase control for the converter-interfaced renewable energy systems to enhance the reliability of the distance relay. This control scheme firstly calculates the phase difference between operating current and fault current by only using local measurements. Then, the phase difference is eliminated via phase angle adjustment. To verify the effectiveness of the proposed control scheme. The performance of the proposed method is tested in a radial three-terminal system and the IEEE 14-bus system in PSCAD/EMTDC.**

***Index Terms*- active phase control, grid-tied converter, distance protection, negative-sequence current injection, renewable energy.**

I. Introduction

Converter-interfaced renewable energy systems (RESs), e.g., the power systems integrated with wind power or photovoltaic solar, are increasing significantly in modern energy systems to address the global challenges on climate change [1][2] In converter-interfaced RESs, the inherent intermittent characteristic of renewable sources and the current limiting of interfaced converters during AC faults may cause the failure of traditional overcurrent protection [3][4].

Although there have been many modified overcurrent protection methods, the relay settings are affected by the system topologies and grid conditions [5]-[8]. Compared with the overcurrent protection, distance protection is unaffected by the limited fault current of converter-interfaced renewable sources and different grid conditions, which can be adopted as alternative backup protection [9]. The distance protection uses local measured current and voltage phasors to calculate the apparent impedance, which reflects the fault distances. However, under the presence of fault resistances, the phase difference between the operating current of the local distance relay and the fault current will cause an error in the apparent impedance[10]. In the conventional power system, synchronous generators (SGs) have similar fault characteristics. The phase difference is small and the apparent impedance error can be effectively solved by applying the quadrilateral characteristic in industrial distance relays [11]. However, in converter-interfaced RESs, the output current of converters is clamped by their fault ride-through (FRT) strategies, which is significantly different from the current of SGs in phase angle [12]. Consequently, the phase difference between the operating current and the fault current is large, which will cause a large measurement error in the apparent impedance [13]. Hence, the distance relay used in the conventional power system is no longer valid for the converter-interfaced RESs.

Different solutions have been proposed to improve the performance of the distance protection in converter-interfaced RESs. Reference [14] proposed a scheme to block the converter-side relay until the action of the remote-end relay, which reduces the effect of phase difference on fault identification. Reference [15] introduced additional differential protection coping with the distance protection to detect the phase-to-phase-to-ground (PPG) faults, while the method requires high-bandwidth communication channels. By calculating the phase difference between the operating current and the fault current during internal faults, reference [16] modified the distance protection algorithm to eliminate the impedance error. However, this solution did not consider external faults with fault resistances. Reference [17] designed an adaptive tripping boundary to resist various pre-fault conditions. But this method requires complicated traversal operation and only the single-phase-to-ground (SPG) faults are considered. The investigation of phase-to-phase (PP) and PPG faults is ignored. Generally, the above protection schemes can enhance the reliability of distance protection in converter-interfaced RESs to a certain extent. However, all of these require the modification of well-established distance relay devices.

To avoid modifying distance relays which is difficult in practical projects, reference [18] proposed an FRT control strategy to mimic the fault features of SGs. This method reduces the phase difference between the operating current and the fault current that affects the distance relay. But the performance of the distance protection under external faults with different fault resistances was not investigated. Additionally, this approach depends on the offline simulation and needs detailed parameters of the entire system, which is a challenge in practice.

In addition to the control-based solutions presented in [18], an active phase control (APC) method is proposed in this paper. This method calculates the phase difference between the operating current and the fault current based on local measurements. On this basis, the proposed APC can eliminate the phase difference by regulating the converter positive-sequence current.

The rest of the paper is structured as follows. Section II discusses the mal-operation issue of the conventional distance protection in the converter-interfaced RESs. In Section III, the proposed APC and protection scheme are systematically analyzed. Simulation results in PSCAD/EMTDC are provided

This work is sponsored by the National Natural Science Foundation of China (52007075) (Corresponding author: Wang Xiang).

H. Zhang, W. Xiang and J. Wen are with the School of Electrical and Electronic Engineering, Huazhong University of Science and Technology, Wuhan 430074, China (e-mail: zhanghaobo9902@foxmail.com; xiangwang1003@hust.edu.cn; jinyu.wen@hust.edu.cn).

Q. Hong is with the Department of Electronic and Electrical Engineering, University of Strathclyde, G1 1XW, Glasgow, UK. (e-mail: q.hong@strath.ac.uk).

in Section IV to verify the efficiency and robustness of the proposed method under different fault types. And the compatibility considering grid codes is also discussed. Finally, the conclusion is drawn in Section V.

II. Mal-operation Analysis of Conventional Distance Protection

A sample radial three-terminal converter-interfaced renewable energy system is used to study the issue of distance protection. Its topology is shown in Fig. 1. Where T denotes the converter transformer. S_1 and S_2 are two local AC grids.

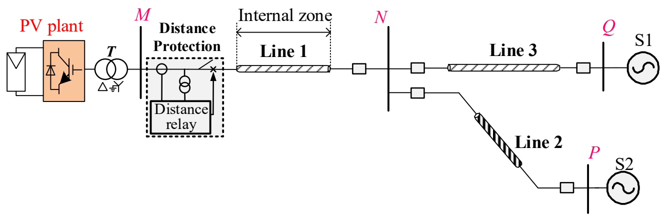

Fig. 1 A radial three-terminal system integrating with PV plant.

The distance relay adopts the commonly used quadrilateral characteristic, which consists of reactance lines of zone 1 and zone 2, resistance line, and directional lines [19], as shown in Fig. 2.

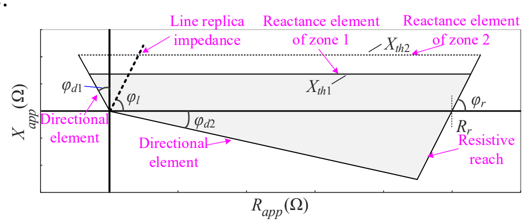

Fig. 2 Quadrilateral characteristic of the adopted distance relay.

Taking M-side distance protection as an example, *line 1* is the primary protected element. Defining the faults located within *line 1* as internal faults, the other faults are referred to be external faults.

1) Internal faults

The equivalent fault circuit of the test system under internal faults is illustrated in Fig. 3. Where F represents the fault location; Z_L represents the line impedance. The symbols with superscripts 'I', 'II', and 'III' respectively denote *line 1, line 2*, and *line 3*. Z_f is the fault impedance from the M-side relay to the fault location. R_f is the fault resistance. x is the fault distance from the relay location (percent form). $\boldsymbol{V}_M$ and $\boldsymbol{I}_M$ denote the measured voltage and current at M-side. $\boldsymbol{I}_F$ represents the fault current at the fault point.

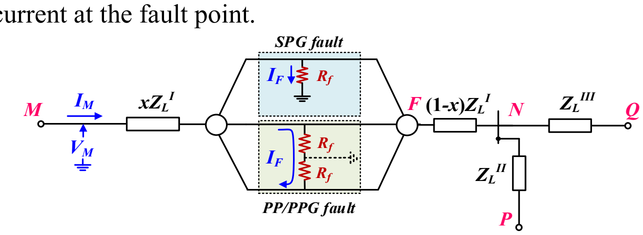

Fig. 3 Equivalent circuit under internal faults.

According to [20], the apparent impedance Z_{app} calculated by the M-side relay under different fault types can be expressed as:

$$Z_{app}=\frac{\boldsymbol{V}_{rM}}{\boldsymbol{I}_{rM}}=\underbrace{xZ_L^I}_{Z_F}+\underbrace{R_f\left(\frac{\boldsymbol{I}_F}{\boldsymbol{I}_{rM}}\right)}_{Z_{ad}} \tag{1}$$

where $\boldsymbol{I}_{rM}$ and $\boldsymbol{V}_{rM}$ are the operating current phasor and voltage phasor for the M-side relay respectively. $\boldsymbol{I}_F$ represents the fault current. The expressions of $\boldsymbol{I}_{rM}$, $\boldsymbol{V}_{rM}$ and $\boldsymbol{I}_F$ under different fault types are provided in Table 1. Where subscripts A, B and C represent phase A, phase B, and phase C, respectively. $\boldsymbol{k}_0$ is the zero-sequence compensation factor of *line 1*, which is defined as:

$$\boldsymbol{k}_0=\frac{Z_{L0}^I-Z_{L1}^I}{Z_{L1}^I} \tag{2}$$

where subscripts '0', '1' and '2' represent the zero-sequence, the positive-sequence and negative-sequence components respectively.

Table 1 Expressions of I_{rM}, V_{rM} and I_F under different fault types.

Faults types		V_{rM}	I_{rM}	I_F
SPG	AG	V_{MA}	$I_{MA}+k_0I_{M0}$	I_{FA}
	BG	V_{MB}	$I_{MB}+k_0I_{M0}$	I_{FB}
	CG	V_{MC}	$I_{MC}+k_0I_{M0}$	I_{FC}
PP/PPG	AB/ABG	$V_{MA}-V_{MB}$	$I_{MA}-I_{MB}$	$I_{FA}-I_{FB}$
	AC/ACG	$V_{MA}-V_{MC}$	$I_{MA}-I_{MC}$	$I_{FA}-I_{FC}$
	BC/BCG	$V_{MB}-V_{MC}$	$I_{MB}-I_{MC}$	$I_{FB}-I_{FC}$

In equation (1), Z_{ad} denotes the additional impedance, which causes Z_{app} to deviate from the actual fault impedance Z_F. As expressed in (1), Z_{ad} is aroused by the fault resistance R_f. Since $\boldsymbol{I}_{rM}$ is affected by the FRT control strategy, $\boldsymbol{I}_{rM}$ is significantly different from the output current of SGs in phase and amplitude, which results in a large phase difference between $\boldsymbol{I}_{rM}$ and $\boldsymbol{I}_F$ [12]. As a result, Z_{ad} in equation (1) has a large reactance part. Under internal faults, the large reactance part of Z_{ad} may force Z_{app} to exceed the action zone of the M-side relay. Fig. 4 depicts two possible mal-operation scenarios. As can be seen, the internal fault is misidentified as external faults. Therefore, the distance relay will not be tripped.

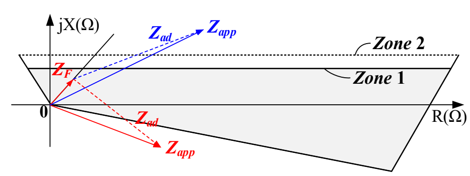

Fig. 4 Apparent impedance by M-side distance relay.

2) External faults

The equivalent circuit of the test system under external faults (faults on *line 3*) is illustrated in Fig. 5.

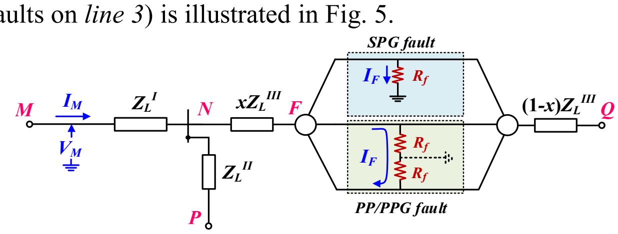

Fig. 5 Equivalent circuit under external faults.

Similar to the analysis under internal faults, the expression of apparent impedance under external faults can be derived as:

$$Z_{app}=\underbrace{Z_L^I+xZ_L^{III}}_{Z_F}+\underbrace{xZ_L^{III}\left(\frac{\boldsymbol{I}_{rP}}{\boldsymbol{I}_{rM}}\right)+R_f\left(\frac{\boldsymbol{I}_F}{\boldsymbol{I}_{rM}}\right)}_{Z_{ad}} \tag{3}$$

where $\boldsymbol{I}_{rP}$ is the operating current of the P-side relay, whose expression is similar to $\boldsymbol{I}_{rM}$. $xZ_L^{III}(\boldsymbol{I}_{rP}/\boldsymbol{I}_{rM})$ in additional impedance is aroused by intermediate infeed current from terminal *P*. For the converter-interfaced RESs, there are still large phase differences between the operating current $\boldsymbol{I}_{rM}$ and the fault current $\boldsymbol{I}_F$. As a result, $R_f(\boldsymbol{I}_F/\boldsymbol{I}_{rM})$ in equation (3) has a large reactance part, which may cause Z_{app} to move inside the action zone of *M*-side relay. As depicted in Fig. 6, the apparent impedance of *M*-side relay falls into zone 1 by mistake. The *M*-side relay will be tripped instantly.

In conclusion, considering fault resistances, the large phase difference between the operating current and the fault current in the converter-interfaced RESs may cause a large error in the reactance part of measured Z_{app}. The distance protection used in conventional SGs-based power systems is no longer valid.

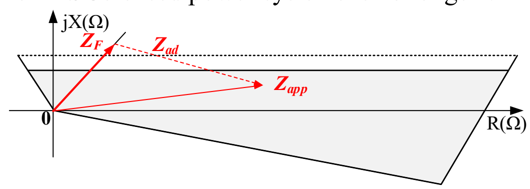

Fig. 6 Apparent impedance by *M*-side distance relay.

III. Enhanced Control-based Distance Protection

To address the mal-operation of distance relay analyzed in Section II, an APC is proposed to mimic the fault current characteristics of SGs by eliminating the phase difference between the operating current and the fault current (defined as δ). As the controlled variable, the phase difference (δ) needs to be calculated in real-time using local measurements.

In the following text, phase-A-to-ground (AG) faults, phase-B-to-phase-C (BC) faults and phase-B-to-phase-C-to-ground (BCG) faults are analyzed as examples of SPG, PP and PPG faults, respectively.

A. Calculation of Phase Difference

1) Internal faults

The expression of δ can be obtained as:

$$\delta = \arg\{\boldsymbol{I}_F\} - \arg\{\boldsymbol{I}_{rM}\} \tag{4}$$

where the phase of $\boldsymbol{I}_{rM}$ can be directly measured by local *M*-side current. But the phase of $\boldsymbol{I}_F$ needs to be calculated. Reference [16] provided a calculation method of $\boldsymbol{I}_F$ under internal faults. According to the conclusion in [16], for internal AG faults, the phase of $\boldsymbol{I}_F$ is:

$$\arg\{\boldsymbol{I}_F\}_{int\_AG} = \arg\left(\Delta\boldsymbol{I}_{M1} \times \frac{\dfrac{\boldsymbol{V}_{M1}^{pre} - \boldsymbol{V}_{M1}^{f}}{\boldsymbol{I}_{M1}^{f} - \boldsymbol{I}_{M1}^{pre}} + Z_{L1}^{I} + \dfrac{Z_{L1}^{II} Z_{L1}^{III}}{Z_{L1}^{II} + Z_{L1}^{III}}}{Z_{L1}^{I}}\right) \tag{5}$$

For internal BC faults, the phase of $\boldsymbol{I}_F$ is:

$$\arg\{\boldsymbol{I}_F\}_{int\_BC} = \arg\left(\Delta\boldsymbol{I}_{M1} \times \frac{\dfrac{\boldsymbol{V}_{M1}^{pre} - \boldsymbol{V}_{M1}^{f}}{\boldsymbol{I}_{M1}^{f} - \boldsymbol{I}_{M1}^{pre}} + Z_{L1}^{I} + \dfrac{Z_{L1}^{II} Z_{L1}^{III}}{Z_{L1}^{II} + Z_{L1}^{III}}}{Z_{L1}^{I}}\right) - 90° \tag{6}$$

For internal BCG faults, the phase of $\boldsymbol{I}_F$ is:

$$\arg\{\boldsymbol{I}_F\}_{int\_BCG} = \arg\left(\begin{array}{c}\Delta\boldsymbol{I}_{M1} \times \dfrac{\dfrac{\boldsymbol{V}_{M1}^{pre} - \boldsymbol{V}_{M1}^{f}}{\boldsymbol{I}_{M1}^{f} - \boldsymbol{I}_{M1}^{pre}} + Z_{L1}^{I} + \dfrac{Z_{L1}^{II} Z_{L1}^{III}}{Z_{L1}^{II} + Z_{L1}^{III}}}{Z_{L1}^{I}} \\ -\Delta\boldsymbol{I}_{M2} \times \dfrac{\dfrac{\boldsymbol{V}_{M2}^{pre} - \boldsymbol{V}_{M2}^{f}}{\boldsymbol{I}_{M2}^{f} - \boldsymbol{I}_{M2}^{pre}} + Z_{L2}^{I} + \dfrac{Z_{L2}^{II} Z_{L2}^{III}}{Z_{L2}^{II} + Z_{L2}^{III}}}{Z_{L2}^{I}}\end{array}\right) - 90° \tag{7}$$

In equations (5)-(7), $\Delta\boldsymbol{I}_{M1} = \boldsymbol{I}_{M1}^{f} - \boldsymbol{I}_{M1}^{pre}$. $\boldsymbol{V}_{M1}$ and $\boldsymbol{I}_{M1}$ are *M*-side positive-sequence voltage and current phasors. Superscripts '*pre*' and '*f*' respectively represent the electrical quantities before and after fault occurrence. The meanings of other symbols are the same as those in Fig. 3.

2) External faults

For external faults (e.g., faults on *line 3*), due to the influence of the intermediate infeed current from terminal *P* as shown in Fig. 5, the analysis in [16] loses its applicability. Thus, the phase calculation formulas for $\boldsymbol{I}_F$ need to be re-derived.

The positive-sequence equivalent circuits of the test system under external faults are depicted in Fig. 7. Where the positive-sequence model of the conventional power grid (S_1 and S_2 in Fig. 1) is represented by a voltage source ($\boldsymbol{E}_G^1$ and $\boldsymbol{E}_G^2$ in Fig. 7) in series with an impedance (Z_G^1 and Z_G^2 in Fig. 7). The PV plant is considered as a voltage-controlled current source (I_M) in series with an impedance of transformer (X_T). Thus, the positive-sequence equivalent circuits before and during the fault are obtained, as shown in Fig. 7 (a) and (b). Where, the superscripts '*pre*' and '*f*' denote the electrical quantities before and during the fault, respectively.

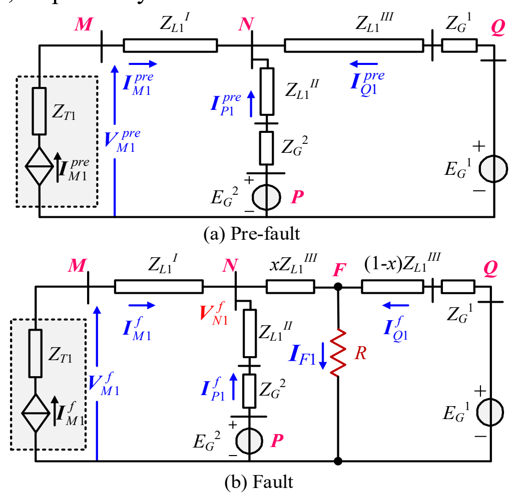

Fig. 7 Positive-sequence equivalent circuit during an external fault.

As analyzed in [21], using the superposition theorem, the fault state can be decomposed into the superposition of the pre-fault state and the additional fault (pure-fault) state. The additional fault network with the pure-fault component is illustrated in Fig. 8 (a). The excitation voltage $\boldsymbol{V}_{F1}^{pf}$ in the pure-fault network is the opposite of $\boldsymbol{V}_{F1}^{pre}$ during the pre-fault state. According to Fig. 8, the change of currents before and after the fault at different terminals can be written as:

$$\begin{cases}\Delta\boldsymbol{I}_{M1} = \boldsymbol{I}_{M1}^{f} - \boldsymbol{I}_{M1}^{pre} \\ \Delta\boldsymbol{I}_{P1} = \boldsymbol{I}_{P1}^{f} - \boldsymbol{I}_{P1}^{pre} \\ \Delta\boldsymbol{I}_{Q1} = \boldsymbol{I}_{Q1}^{f} - \boldsymbol{I}_{Q1}^{pre}\end{cases} \tag{8}$$

It should be noted that, under a specific control scheme, the change of PV plant's current ΔI_{M1} is dependent on the variation of terminal voltage ΔV_{M1} [22]. If no fault occurs, $\Delta V_{M1}=\Delta I_{M1}=0$. Thus, the current source ΔI_{M1} in Fig. 8 (a) operates as a passive non-linear load. On this basis, the equivalent circuit of Fig. 8 (b) can be obtained. Where Z_{R1}^{pf} is the equivalent impedance of PV plant during the pure-fault state, which is affected by control system and fault conditions [15].

From Fig. 8 (b), ΔI_{M1} can be expressed as:

$$\Delta \boldsymbol{I}_{M1} = \frac{\boldsymbol{I}_{F1} \times \left((1-x)Z_{L1}^{III} + Z_G^1\right)(Z_{L1}^{II} + Z_G^2)}{(Z_{L1}^{III} + Z_G^1)(Z_{R1}^{pf} + Z_{L1}^{I} + Z_{L1}^{II} + Z_G^2) + (Z_{R1}^{pf} + Z_{L1}^{I})(Z_{L1}^{II} + Z_G^2)} \quad (9)$$

where $\boldsymbol{I}_{F1}=\boldsymbol{I}_{M1}^{f}+\boldsymbol{I}_{P1}^{f}+\boldsymbol{I}_{Q1}^{f}$. In addition, Z_{R1}^{pf} can be obtained:

$$Z_{R1}^{pf} = \frac{1}{(\boldsymbol{I}_{M1}^{f} - \boldsymbol{I}_{M1}^{pre})}\left(\boldsymbol{V}_{M1}^{pre} - \boldsymbol{V}_{M1}^{f}\right) \quad (10)$$

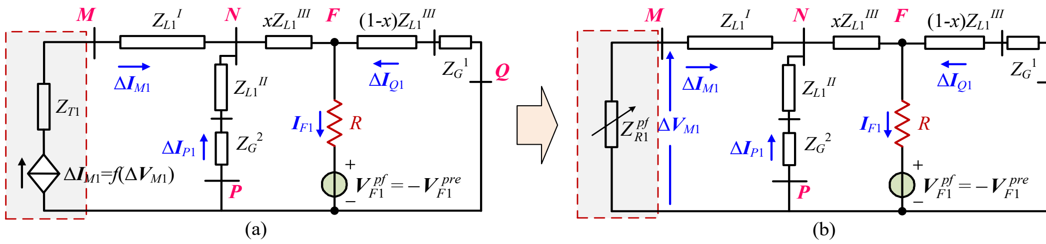

Fig. 8 Pure-fault superposition network during an external fault.

In equation (9), the equivalent grid impedance is much smaller than those of lines and PV plants [16]. Ignoring the equivalent impedance of AC system Z_G^1, Z_G^2, and substituting (10) into (9), the positive-sequence fault current $\boldsymbol{I}_{F1}$ can be obtained:

$$\boldsymbol{I}_{F1} = \Delta \boldsymbol{I}_{M1} \times \frac{Z_{R1}^{pf} + Z_{L1}^{I} + \dfrac{Z_{L1}^{II} Z_{L1}^{III}}{Z_{L1}^{II} + Z_{L1}^{III}}}{\dfrac{(1-x)Z_{L1}^{II} Z_{L1}^{III}}{Z_{L1}^{II} + Z_{L1}^{III}}} \quad (11)$$

a) Phase-A-to-ground faults

For external AG faults, the relationship between the sequence current and fault current is $\boldsymbol{I}_F = 3\boldsymbol{I}_{F1}$. Hence, the phase of $\boldsymbol{I}_F$ can be calculated as:

$$\arg\{\boldsymbol{I}_F\}_{ext\_AG} = \arg\left(\Delta \boldsymbol{I}_{M1} \times \frac{Z_{R1}^{pf} + Z_{L1}^{I} + \dfrac{Z_{L1}^{II} Z_{L1}^{III}}{Z_{L1}^{II} + Z_{L1}^{III}}}{\dfrac{(1-x)Z_{L1}^{II} Z_{L1}^{III}}{Z_{L1}^{II} + Z_{L1}^{III}}}\right) \quad (12)$$

b) Phase-B-to-Phase-C faults

According to Table 1, under BC/BCG faults, $\boldsymbol{I}_F = \boldsymbol{I}_{FB} - \boldsymbol{I}_{FC} = \sqrt{3}\, e^{-j90°}(\boldsymbol{I}_{F1} - \boldsymbol{I}_{F2})$. For external BC faults, $\boldsymbol{I}_{F1} = -\boldsymbol{I}_{F2}$, the phase of $\boldsymbol{I}_F$ can be expressed as:

$$\arg\{\boldsymbol{I}_F\}_{ext\_BC} = \arg\left(\Delta \boldsymbol{I}_{M1} \times \frac{Z_{R1}^{pf} + Z_{L1}^{I} + \dfrac{Z_{L1}^{II} Z_{L1}^{III}}{Z_{L1}^{II} + Z_{L1}^{III}}}{\dfrac{(1-x)Z_{L1}^{II} Z_{L1}^{III}}{Z_{L1}^{II} + Z_{L1}^{III}}}\right) - 90° \quad (13)$$

c) Phase-B-to-Phase-C-to-ground faults

For external BCG faults, the negative-sequence fault current $\boldsymbol{I}_{F2}$ needs to be determined. Similar to the calculation principle of $\boldsymbol{I}_{F1}$, $\boldsymbol{I}_{F2}$ can be calculated as:

$$\boldsymbol{I}_{F2} = \Delta \boldsymbol{I}_{M2} \times \frac{Z_{R2}^{pf} + Z_{L2}^{I} + \dfrac{Z_{L2}^{II} Z_{L2}^{III}}{Z_{L2}^{II} + Z_{L2}^{III}}}{\dfrac{(1-x)Z_{L2}^{II} Z_{L2}^{III}}{Z_{L2}^{II} + Z_{L2}^{III}}} \quad (14)$$

where

$$\Delta \boldsymbol{I}_{M2} = \boldsymbol{I}_{M2}^{f} - \boldsymbol{I}_{M2}^{pre} \quad (15)$$

$$Z_{R2}^{pf} = \frac{1}{\boldsymbol{I}_{M2}^{f} - \boldsymbol{I}_{M2}^{pre}}\left(\boldsymbol{V}_{M2}^{pre} - \boldsymbol{V}_{M2}^{f}\right) \quad (16)$$

Thus, the phase of $\boldsymbol{I}_F$ under external BCG faults can be expressed as:

$$\arg\{\boldsymbol{I}_F\}_{ext\_BCG} = \arg\left(\begin{array}{l} \Delta \boldsymbol{I}_{M1} \times \dfrac{Z_{R1}^{pf} + Z_{L1}^{I} + \frac{Z_{L1}^{II} Z_{L1}^{III}}{Z_{L1}^{II} + Z_{L1}^{III}}}{\frac{(1-x)Z_{L1}^{II} Z_{L1}^{III}}{Z_{L1}^{II} + Z_{L1}^{III}}} \\ -\Delta \boldsymbol{I}_{M2} \times \dfrac{Z_{R2}^{pf} + Z_{L2}^{I} + \frac{Z_{L2}^{II} Z_{L2}^{III}}{Z_{L2}^{II} + Z_{L2}^{III}}}{\frac{(1-x)Z_{L2}^{II} Z_{L2}^{III}}{Z_{L2}^{II} + Z_{L2}^{III}}} \end{array}\right) - 90° \quad (17)$$

In summary, the phase of $\boldsymbol{I}_F$ under internal and external faults can be concluded in Table 2.

Table 2 Phase of fault current I_F under internal and external faults.

Fault types	$\arg\{\boldsymbol{I}_F\}$ Internal	$\arg\{\boldsymbol{I}_F\}$ External
BC	$\arg\left(\Delta \boldsymbol{I}_{M1} \times \dfrac{\frac{\boldsymbol{V}_{M1}^{pre} - \boldsymbol{V}_{M1}^{f}}{\boldsymbol{I}_{M1}^{f} - \boldsymbol{I}_{M1}^{pre}} + Z_{L1}^{I} + \frac{Z_{L1}^{II} Z_{L1}^{III}}{Z_{L1}^{II} + Z_{L1}^{III}}}{Z_{L1}^{I}}\right) - 90°$	$\arg\left(\Delta \boldsymbol{I}_{M1} \times \dfrac{\frac{\boldsymbol{V}_{M1}^{pre} - \boldsymbol{V}_{M1}^{f}}{\boldsymbol{I}_{M1}^{f} - \boldsymbol{I}_{M1}^{pre}} + Z_{L1}^{I} + \frac{Z_{L1}^{II} Z_{L1}^{III}}{Z_{L1}^{II} + Z_{L1}^{III}}}{\frac{(1-x)Z_{L1}^{II} Z_{L1}^{III}}{Z_{L1}^{II} + Z_{L1}^{III}}}\right) - 90°$
BCG	$\arg\left(\begin{array}{l} \Delta \boldsymbol{I}_{M1} \times \dfrac{\frac{\boldsymbol{V}_{M1}^{pre} - \boldsymbol{V}_{M1}^{f}}{\boldsymbol{I}_{M1}^{f} - \boldsymbol{I}_{M1}^{pre}} + Z_{L1}^{I} + \frac{Z_{L1}^{II} Z_{L1}^{III}}{Z_{L1}^{II} + Z_{L1}^{III}}}{Z_{L1}^{I}} \\ -\Delta \boldsymbol{I}_{M2} \times \dfrac{\frac{\boldsymbol{V}_{M2}^{pre} - \boldsymbol{V}_{M2}^{f}}{\boldsymbol{I}_{M2}^{f} - \boldsymbol{I}_{M2}^{pre}} + Z_{L2}^{I} + \frac{Z_{L2}^{II} Z_{L2}^{III}}{Z_{L2}^{II} + Z_{L2}^{III}}}{Z_{L2}^{I}} \end{array}\right) - 90°$	$\arg\left(\begin{array}{l} \Delta \boldsymbol{I}_{M1} \times \dfrac{\frac{\boldsymbol{V}_{M1}^{pre} - \boldsymbol{V}_{M1}^{f}}{\boldsymbol{I}_{M1}^{f} - \boldsymbol{I}_{M1}^{pre}} + Z_{L1}^{I} + \frac{Z_{L1}^{II} Z_{L1}^{III}}{Z_{L1}^{II} + Z_{L1}^{III}}}{\frac{(1-x)Z_{L1}^{II} Z_{L1}^{III}}{Z_{L1}^{II} + Z_{L1}^{III}}} \\ -\Delta \boldsymbol{I}_{M2} \times \dfrac{\frac{\boldsymbol{V}_{M2}^{pre} - \boldsymbol{V}_{M2}^{f}}{\boldsymbol{I}_{M2}^{f} - \boldsymbol{I}_{M2}^{pre}} + Z_{L2}^{I} + \frac{Z_{L2}^{II} Z_{L2}^{III}}{Z_{L2}^{II} + Z_{L2}^{III}}}{\frac{(1-x)Z_{L2}^{II} Z_{L2}^{III}}{Z_{L2}^{II} + Z_{L2}^{III}}} \end{array}\right) - 90°$

AG	$\arg\left(\Delta \boldsymbol{I}_{M1}\times\dfrac{\dfrac{\boldsymbol{V}_{M1}^{pre}-\boldsymbol{V}_{M1}^{f}}{\boldsymbol{I}_{M1}^{f}-\boldsymbol{I}_{M1}^{pre}}+Z_{L1}^{I}+\dfrac{Z_{L1}^{II}Z_{L1}^{III}}{Z_{L1}^{II}+Z_{L1}^{III}}}{Z_{L1}^{I}}\right)$	$\arg\left(\Delta \boldsymbol{I}_{M1}\times\dfrac{\dfrac{\boldsymbol{V}_{M1}^{pre}-\boldsymbol{V}_{M1}^{f}}{\boldsymbol{I}_{M1}^{f}-\boldsymbol{I}_{M1}^{pre}}+Z_{L1}^{I}+\dfrac{Z_{L1}^{II}Z_{L1}^{III}}{Z_{L1}^{II}+Z_{L1}^{III}}}{\dfrac{(1-x)Z_{L1}^{II}Z_{L1}^{III}}{Z_{L1}^{II}+Z_{L1}^{III}}}\right)$

As can be seen from Table 2, the phase of fault current I_F only differs in the denominator of each equation under internal and external faults. Since the positive and negative-sequence impedances of each line are considered to be the same, we can get:

$$\arg(Z_{L1}^{I})=\arg(Z_{L2}^{I})=\arg\left(\frac{(1-x)Z_{L1}^{II}Z_{L1}^{III}}{Z_{L1}^{II}+Z_{L1}^{III}}\right)=\arg\left(\frac{(1-x)Z_{L2}^{II}Z_{L2}^{III}}{Z_{L2}^{II}+Z_{L2}^{III}}\right) \quad (18)$$

Therefore,

$$\begin{cases}\arg\{\boldsymbol{I}_F\}_{int\_AG}=\arg\{\boldsymbol{I}_F\}_{ext\_AG}\\ \arg\{\boldsymbol{I}_F\}_{int\_BC}=\arg\{\boldsymbol{I}_F\}_{ext\_BC}\\ \arg\{\boldsymbol{I}_F\}_{int\_BCG}=\arg\{\boldsymbol{I}_F\}_{ext\_BCG}\end{cases} \quad (19)$$

As shown in equation (19), the calculation of $\boldsymbol{I}_F$ is universal for both internal and external faults. Only adopting equation (5) -(7), the phase of $\boldsymbol{I}_F$ at any fault location can be determined using local measurements. Therefore, the phase difference δ can be obtained through equation (4).

B. Active phase control

The APC aims to eliminate the phase difference δ by controlling the operating current phasor $\boldsymbol{I}_{rM}$ to align with fault current phasor $\boldsymbol{I}_F$. Where $\boldsymbol{I}_{rM}$ can be further expressed by M-side positive-sequence current $\boldsymbol{I}_{M1}$, negative-sequence current $\boldsymbol{I}_{M2}$, and zero-sequence current $\boldsymbol{I}_{M0}$.

$$\boldsymbol{I}_{rM}=\begin{cases}\boldsymbol{I}_{MB}-\boldsymbol{I}_{MC}=\sqrt{3}e^{-j90^\circ}\left(\boldsymbol{I}_{M1}-\boldsymbol{I}_{M2}\right) & ,BC/BCG\ \ faults.\\ \boldsymbol{I}_{MA}+\boldsymbol{k}_0\boldsymbol{I}_{M0}=\boldsymbol{I}_{M1}+\boldsymbol{I}_{M2}+(1+\boldsymbol{k}_0)\boldsymbol{I}_{M0} & ,AG\ \ faults.\end{cases} \quad (20)$$

Since M-side zero-sequence current flows through the ground of the converter transformer, $\boldsymbol{I}_{M0}$ is constant and unaffected by converter control. The negative-sequence current $\boldsymbol{I}_{M2}$ is usually determined by the requirements of the grid codes. Mostly, the negative-sequence current is suppressed to make full use of the current capacity [23]-[25]. While for some grid codes with the requirement of negative-sequence current injection, the desired negative-sequence reactive current is proportional to the negative-sequence voltage [26][27]. However, no matter which grid code $\boldsymbol{I}_{M2}$ can be regarded as a fixed phasor during the steady-state of negative-sequence current control. The phase of $\boldsymbol{I}_{rM}$ can be adjusted by regulating the positive-sequence phasor $\boldsymbol{I}_{M1}$. Fig. 9 presents the basic principle of the adjustment in the synchronous reference frame. The phasors with superscripts '(0)' and '(1)' represent the phasors before and after adjustment.

The θ is the desired adjustment angle. And φ is the power factor (PF) angle of the converter before adjustment, which is dependent on the FRT strategies.

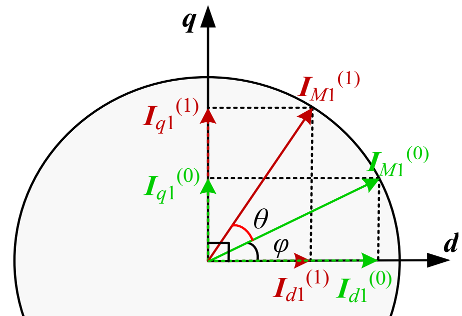

Fig. 9 Control principle of phase adjustment method.

As shown in Fig. 9, to increase the phase of $\boldsymbol{I}_{M1}$ by θ, the desired positive-sequence current references of converter control can be obtained as:

$$\begin{cases}I_{d1}^{*}=\boldsymbol{I}_{d1}^{(1)}=I_{M1}\cdot\cos(\varphi+\theta)\\ I_{q1}^{*}=\boldsymbol{I}_{q1}^{(1)}=I_{M1}\cdot\sin(\varphi+\theta)\end{cases} \quad (21)$$

where I_{M1} is the upper limit of current control.

Based on the principle shown in Fig. 9, a PI controller is adopted in the APC method to control the phase of $\boldsymbol{I}_{rM}$ dynamically. Different from equation (21), the adjustment angle θ is generated by PI controller. θ is designed as:

$$\theta=k_p\left(\delta-0\right)+k_i\int\left(\delta-0\right)dt \quad (22)$$

Consequently, the phase difference δ can be adjusted to its reference value (0) in steady-state through PI controller. The corresponding positive-sequence current references can be simplified as:

$$\begin{cases}I_{d1}^{*}=I_{M1}\cdot\cos\left(k_p\left(\delta-0\right)+k_i\int\left(\delta-0\right)dt\right)\\ I_{q1}^{*}=I_{M1}\cdot\sin\left(k_p\left(\delta-0\right)+k_i\int\left(\delta-0\right)dt\right)\end{cases} \quad (23)$$

where the phase difference δ can be obtained by the calculation method presented in Section III.A. On this basis, the control diagram of the APC can be designed, as shown in Fig. 10. When the fault types are identified, the phase adjustment control is switched on to generate positive-sequence current references.

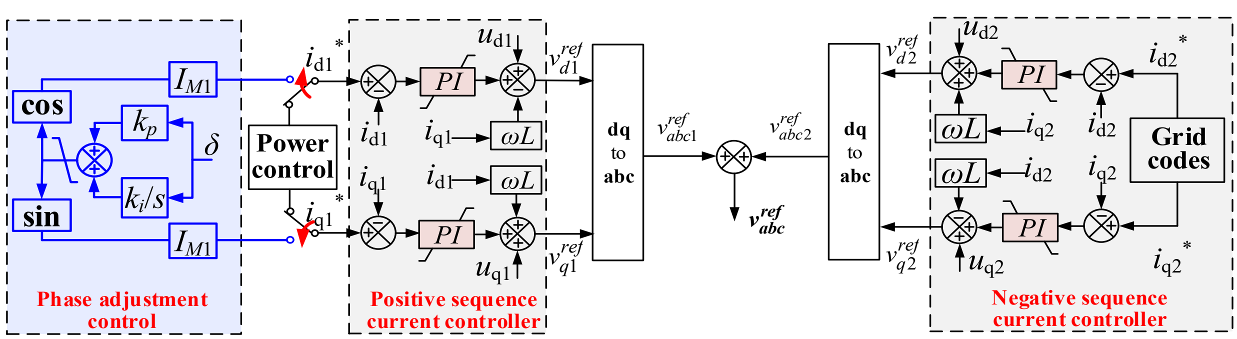

Fig. 10 The proposed active phase control.

C. Compatibility of the APC Method under Grid Codes

According to modern grid codes, interfaced converters are required to generate sufficient reactive power to support grid voltage under the faults. Meanwhile, some strict grid codes require the converters to inject negative-sequence current into the power grid, such as the German code [26]-[29]. Under the above requirements of grid codes, the compatibility of the proposed APC method is discussed below:

- As analyzed before, the APC has a similar phase feature to the output current of SGs, which can achieve a small phase difference between operating current and fault current. Thus, the APC can generate a sufficient reactive current like SGs, which also meets grid codes' reactive power generation requirement.
- The APC method is implemented through positive-sequence control, which has no effect on the negative-sequence current injection of converters. Moreover, according to Table 2, the phase difference calculation of APC method is still available under negative-sequence current injection. Therefore, the APC method is still applicable to locate the fault and generate negative-sequence current even under the grid codes with the requirement of negative-sequence current injection.

In summary, the APC method is suitable for converters under modern grid codes. Based on the proposed APC, the overall flowchart of the distance protection is concluded in Fig. 11.

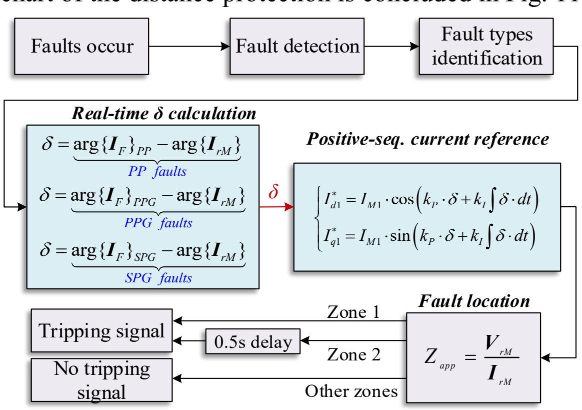

Fig. 11 Flowchart of the proposed protection scheme.

IV. Simulation Verification

A three-terminal medium-voltage system displayed in Fig. 1 is built in PSCAD/EMTDC. The parameters of this system are listed in Table 3. During steady-state, the PV inverter is controlled to generate maximum active power using the Maximum Power Point Tracking algorithm at unity power factor (PF) [18]. Considering most grid codes do not require negative-sequence current injection, similar to existing literature, the negative-sequence current is suppressed [10][15][23]-[25].

Taking the M-side distance relay as an example, the parameters of the quadrilateral characteristic shown in Fig. 2 are designed according to reference [30]. The reach setting (protected range) of zone 1 is set to be 85% of line 1. The reactive reach of zone 1 (X_{th1}) is set as 13.34 Ω, which is equal to the product of the length of zone 1 and the reactance part of Z_{L1}. In the same way, the reactive reach of zone 2 (X_{th2}) is set to be 18.83 Ω, indicating zone 2 of the M-side relay protects 120% of line 1. The resistive reach R_r is set to ensure that the distance protection does not trip for heavy power flow. Referring to the design standard [31], the R_r is set to 100 **Ω**. The tilt angle of the line replica impedance line is equal to the impedance angle of the transmission line. Besides, referring to the distance relay in [30], the parameters of other lines of the quadrilateral characteristic are set to be the recommended values. The basic parameters of the quadrilateral characteristic are concluded in Table 4.

Table 3 The basic parameters of the tested system.

Parameters	***Value***	***Parameters***	***Value***
AC voltage V_n	35kV	Positive-sequence line impedance Z_{L1}	0.132+j0.31387 Ω/km
AC frequency f_n	50Hz	Zero-sequence line impedance Z_{L0}	0.132+j0.94161 Ω/km
Rated capacity of PV plant S_{rated}	6MVA	Length of line 1 L_1	50km
Power to S1	2MVA	Length of line 2 L_2	25km
Power to S2	4MVA	Length of line 3 L_3	50km

To verify the performance of the proposed APC method, the faults with different fault resistances are applied in different locations. For the cases discussed in the following, the faults all occur at 3.0s. Considering the duration of fault detection and identification, the APC is activated at 3.005s [32].

Table 4 The basic parameters of the quadrilateral characteristic.

Parameters	***Value***
Reactance reach of zone 1 (X_{th1})	13.34 Ω
Reactance reach of zone 2 (X_{th2})	18.83 Ω
φ_{d1}	25°
φ_{d2}	15°
φ_l	67.19°
φ_l	67.19°
R_r	100 Ω

A. Verification of δ Calculation

1) Internal faults

Permanent BC, BCG and AG faults with 20Ω and 40Ω resistances are applied 25km away from the M-side distance relay. To study the accuracy of δ calculation, the proposed APC is not activated during faults. The phase difference δ is calculated by equations (4)-(7). Fig. 12 shows the calculated phase difference δ_c and the actual phase difference δ_t.

As can be seen in Fig. 12, since the voltage and current phasor are measured by full-cycle discrete Fourier transform [33], the calculated phase difference δ_c is not accurate during the first cycle. Whereas, after about two fundamental frequency cycles (40ms), the calculated δ is highly consistent with the actual value. The maximum error is only 2°. Moreover, the calculation equations under internal faults are robust to different fault resistances.

2) External faults

Permanent BC, BCG, and AG faults with 20Ω and 40Ω resistances are applied 55km away from the M-side relay (on line 3). The APC is still disabled. To verify equation (19), the equations under internal and external faults in Table 2 are both used to calculate δ. Define δ_{c1} as the phase difference calculated by equations (5)-(7), and δ_{c2} as the phase difference calculated by equations (12), (13) and (17). The calculated phase difference δ_{c1} and δ_{c2} and the actual phase difference δ_t are shown in Fig. 13.

As can be seen, the calculated δ_{c1} and the calculated δ_{c2} are the same. Thus, the correctness of equation (19) is verified. Besides, the calculated results are also highly consistent with the actual value after about two fundamental frequency cycles. The maximum error is only 2°.

B. Verification of the Proposed APC Method

1) Zone 1 Faults

a) Faults inside zone 1: BC, BCG and AG faults with 20Ω fault resistance are applied 25km away from the *M*-side distance relay. The performance of the proposed protection scheme is shown in Fig. 14.

Fig. 14 (a) and (d) show the control and identification results under BC fault, respectively. As can be seen in Fig. 14 (a), the proposed APC is activated at 3.005s. And the phase of the $\boldsymbol{I}_{rM}$ is finally regulated to be the same as the phase of $\boldsymbol{I}_F$ at 3.025ms. Meanwhile, the measured Z_{app} in Fig. 14 (d) converges to point (38.28+ j8.14 Ω). Compared to the actual fault reactance (7.85 Ω), the error of the reactance is only 0.29Ω (4% error rate). The simulation results under BCG fault are shown in Fig. 14 (b) and (e). The phase of $\boldsymbol{I}_{rM}$ can also be adjusted to be equal to the phase of $\boldsymbol{I}_F$ at 3.025ms. The measured Z_{app} in Fig. 14 (e) is 37.36+*j*7.82 Ω, which only has an error of 0.03Ω in the reactance part.

Fig. 14 (c) and (f) show the simulation results under an AG fault at 25km. As shown in Fig. 14 (c), the phase of $\boldsymbol{I}_{rM}$ is controlled to be equal to the phase of I_F at 3.025ms. At the same time, the measured Z_{app} in Fig. 14 (f) is 28.56+ *j*8.15 Ω. The error in the reactance is only 0.3Ω (4% error).

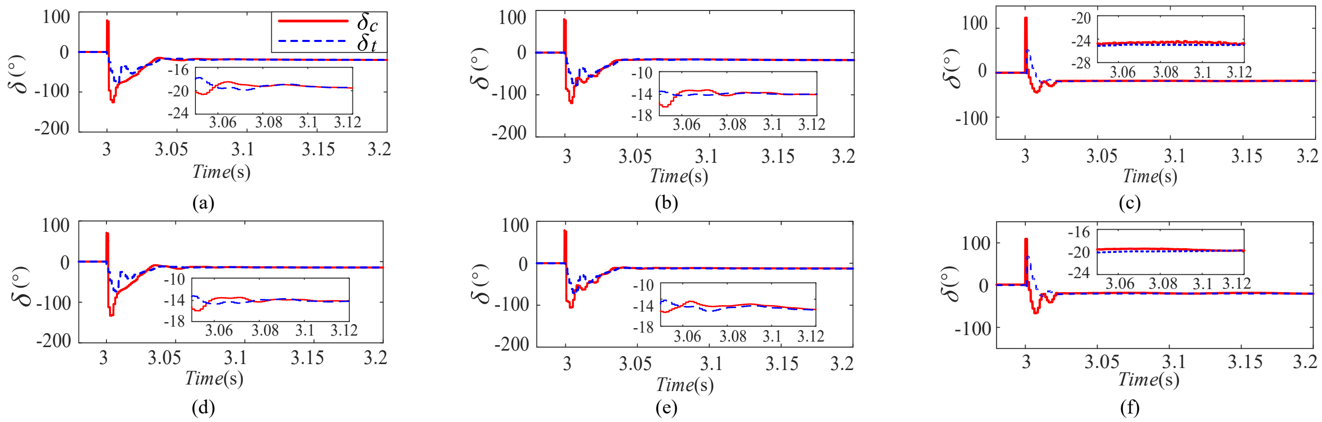

Fig. 12 Calculated and actual δ under different faults at 25km from *M*-side distance relay. (a) BC, R_f= 20Ω. (b) BCG, R_f= 20Ω. (c) AG, R_f= 20Ω. (d) BC, R_f= 40Ω. (e) BCG, R_f= 40Ω. (f) AG, R_f= 40Ω.

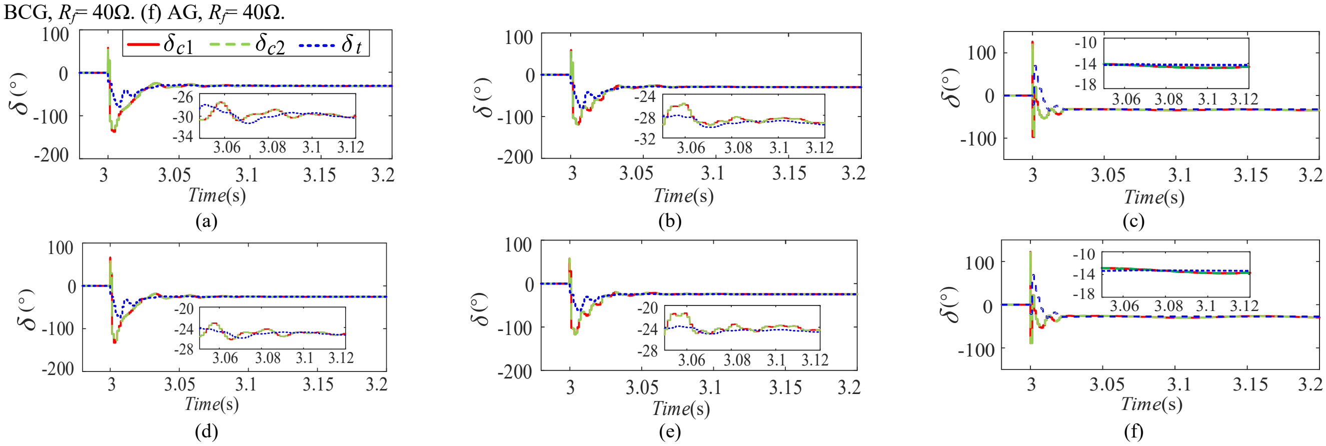

Fig. 13 Calculated and actual δ under different faults at 55km from *M*-side relay. (a) BC, R_f= 20Ω. (b) BCG, R_f= 20Ω. (c) AG, R_f= 20Ω. (d) BC, R_f= 40Ω. (e) BCG, R_f= 40Ω. (f) AG, R_f= 40Ω.

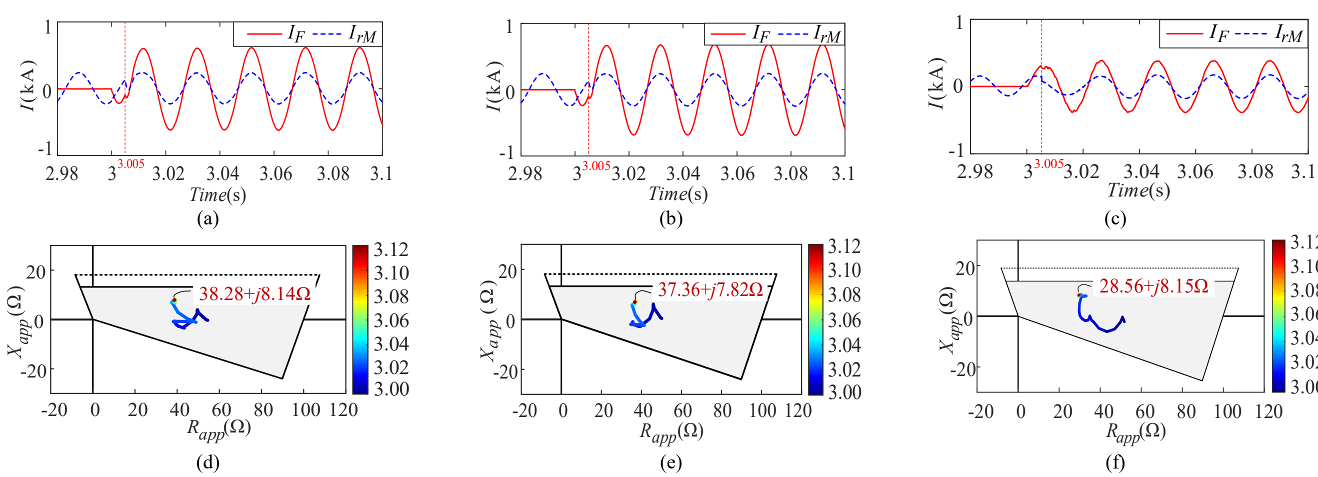

Fig. 14 Performance under faults at 25km. (a) I_F and I_{rM} under BC fault. (b) I_F and I_{rM} under BCG fault. (c) I_F and I_{rM} under AG fault. (d) Measured Z_{app} under BC fault. (e) Measured Z_{app} under BCG fault. (f) Measured Z_{app} under AG fault.

b) Close-in faults: To verify the performance of APC under close-in faults, BC, BCG and AG faults with 20Ω resistance are applied at the *M*-side relay. As shown in Fig. 15, the measured Z_{app} can enter zone 1 within 20ms and remain in that zone for the entire duration of the fault. Hence, the *M*-side relay can be tripped quickly when the close-in faults happen.

c) Faults at reach setting of zone 1: As mentioned before, the relay reach setting of zone 1 is 85% of line 1. To investigate the performance of the proposed APC methods under the critical scenario, the BC, BCG and AG faults with 20Ω resistance were applied at 85% of line 1, i.e., 42.5km away from the *M*-side distance relay.

The measured Z_{app} under the above three scenarios is shown in Fig. 16. Compared with the actual fault reactance (13.34 Ω), the maximum error in measured reactance is approximately 3%. Although the BC and AG faults are identified as zone 2 faults, these different identification results are normal in this critical situation.

2) *Zone* 2 *Faults*

a) Faults on line 1: Internal BC, BCG and AG faults are applied 50km away from *the M*-side relay. The fault resistance is 20Ω. The actual fault reactance is 15.69Ω. Fig. 17 depicts the measured Z_{app} under three fault scenarios. As can be seen, the maximum error in the reactance part is only about 0.5Ω (3% error). Therefore, zone 2 faults on *line 1* can be distinguished correctly.

b) Faults on line 3: The external BC, BCG and AG faults with 20Ω resistance are applied inside zone 2 on line 3. The fault location is 55km away from the *M*-side relay.

Fig. 18 (a)-(f) shows the phase difference δ and the measured Z_{app} under BC, BCG and AG faults. Fig. 18 (a)-(c) show that, at 3.025s, the actual phase difference δ_t can be eliminated by adjusting the calculated phase difference δ_c to 0. Meanwhile, Fig. 18 (d)-(f) show the measured Z_{app} can move outside of zone 1 at 25ms after faults occur and rapidly converge to points (46.12+*j*22.03 Ω), (45.97+*j*20.23 Ω) and (42.63+*j*19.11 Ω), respectively. Compared to the actual reactance (17.26Ω), the measured reactance is slightly larger. This difference is mainly caused by the presence of intermediate infeed current $\boldsymbol{I}_{rP}$ in (3), which is reasonable under external faults. Whereas the measured Z_{app} exceeds the zone 2 boundary of 18.83 Ω, and these faults are located outside of zone 2. In fact, the misidentification has no threat to the security of the power system, since the faults will be isolated immediately by distance relay on line 3.

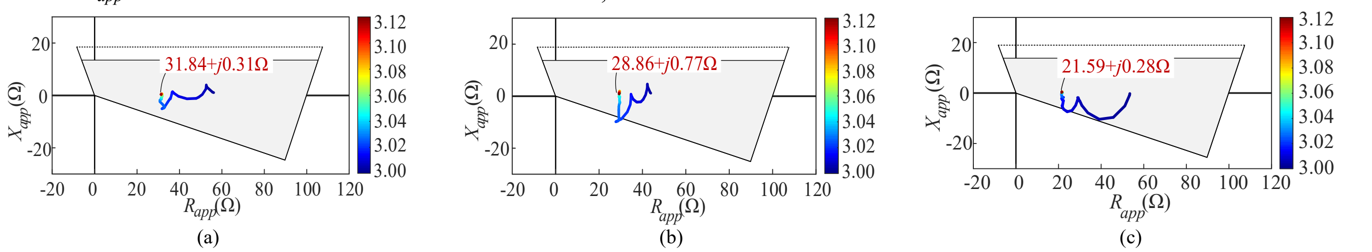

Fig. 15 Performance under close-in faults. (a) BC fault. (b) BCG fault. (c) AG fault.

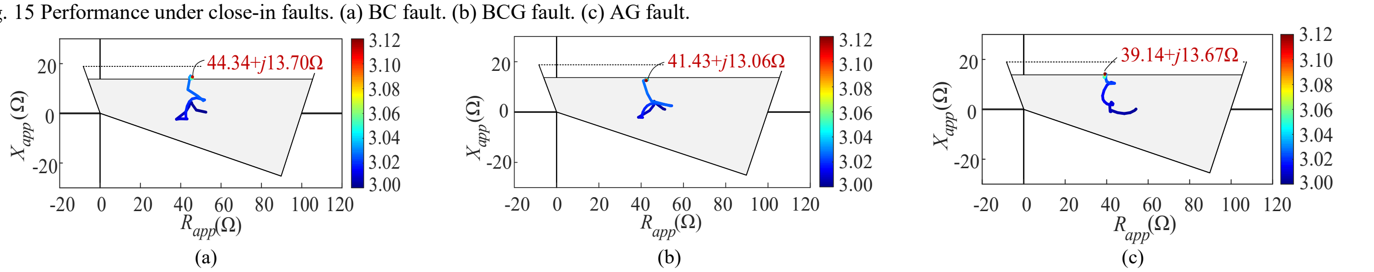

Fig. 16 Performance under the faults at reach setting of zone 1. (a) BC fault. (b) BCG fault. (c) AG fault.

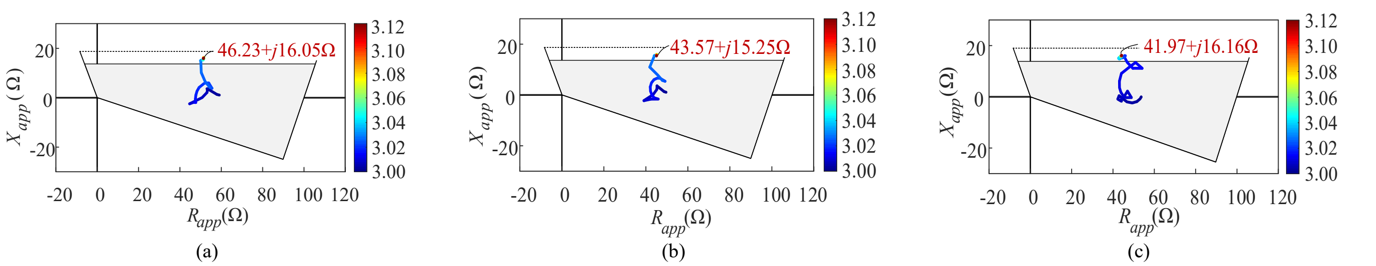

Fig. 17 Performance under zone 2 faults (on line 1). (a) BC fault. (b) BCG fault. (c) AG fault.

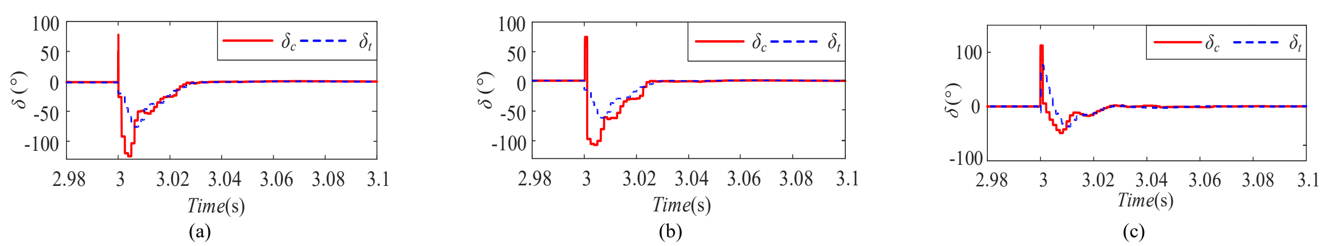

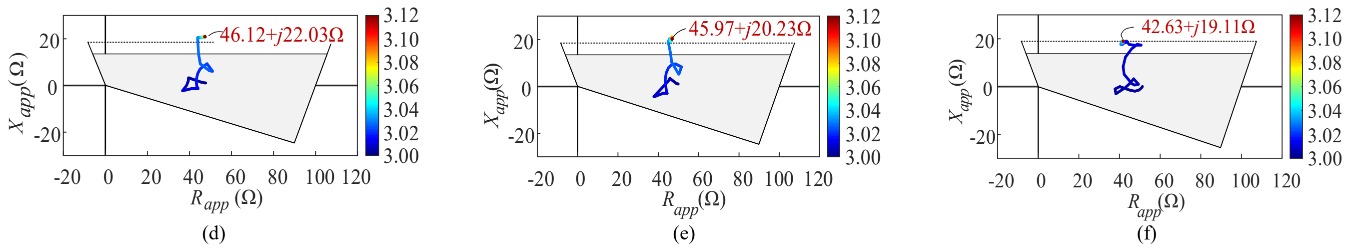

Fig. 18 Performance under zone 2 faults (on line 3). (a) Phase difference δ under BC fault. (b) Phase difference δ during BCG fault. (c) Phase difference δ during AG fault. (d) Measured Z_{app} under BC fault. (e) Measured Z_{app} under BCG fault. (f) Measured Z_{app} under AG fault.

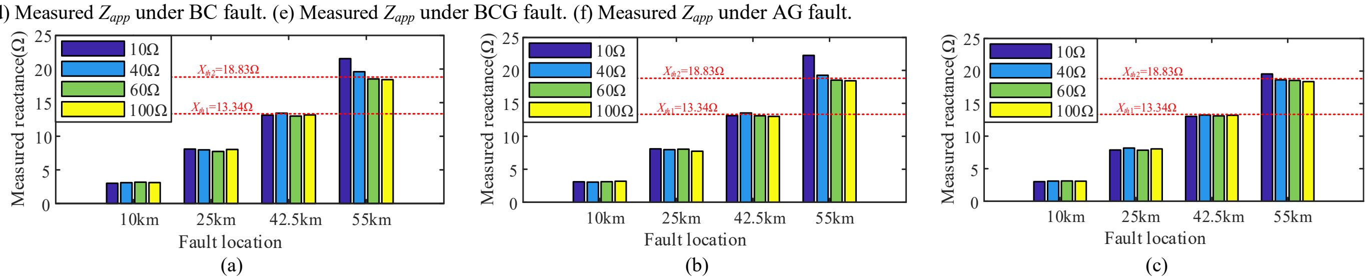

Fig. 19 Measured reactance under (a) BC faults, (b) BCG faults, (c) AG faults with different resistances and locations.

C. Robustness to Fault Resistances

To investigate the robustness of the proposed APC method to different fault resistances, the BC, BCG and AG faults with fault resistances of 10Ω, 40Ω, 60Ω and 100Ω are applied at 10km, 25km, 42.5km, 55km (on line 3) away from the *M*-side relay, respectively. Fig. 19 shows the measured reactance under different fault types.

As can be seen, the measured reactance under internal faults (at 10km, 25km and 42.5km) is accurate and almost unchanged with the increase of fault resistances, which validates that the proposed method is robust to fault resistances. The maximum error rate is less than 4%. For external faults (at 55km), although the measured reactance varies greatly with different fault resistances, the measured reactances are always larger than the actual fault reactance (17.26Ω). Thereby, the external faults will not be identified as zone 1 faults.

D. Compatibility under Grid Codes

To verify the compatibility of the APC under grid codes, the performance considering the German grid code (VDE-AR-N 4120 [26]) is tested. Where the injected negative-sequence reactive current is required to be proportional to the negative-sequence voltage:

$$I_{Q2}^{*} = kV_{t2} \tag{24}$$

where, V_{t2} is the amplitude of terminal negative-sequence voltage, and k is the proportional gain between negative-sequence voltage and reactive current, which varies between 2 and 6. In this paper, k is selected as 2, which means the amplitude of injected negative-sequence reactive current is twice that of negative-sequence voltage (in per unit). According to the controller proposed in [27], the negative-sequence reference can be obtained:

$$\begin{cases} I_{d2}^{*} = kV_{q2} \\ I_{q2}^{*} = kV_{d2} \end{cases} \tag{25}$$

Apply a BCG fault with 100Ω at 25km away from *M*-side relay. Fig. 20 presents the results under the German grid code. As shown in Fig. 20 (a), the phase of the injected negative-sequence current I_{2p} leads to the phase of negative-sequence voltage V_{2p} by 103.39°. Thus, the injected negative-sequence current is predominantly reactive. Moreover, it can be seen from Fig. 20 (b) that the amplitude of the injected negative-sequence current I_{2m} is twice that of the negative-sequence voltage V_{2m}. The above results are fundamentally coincident with the results in [27], which complies with the grid code VDE-AR-N 4120.

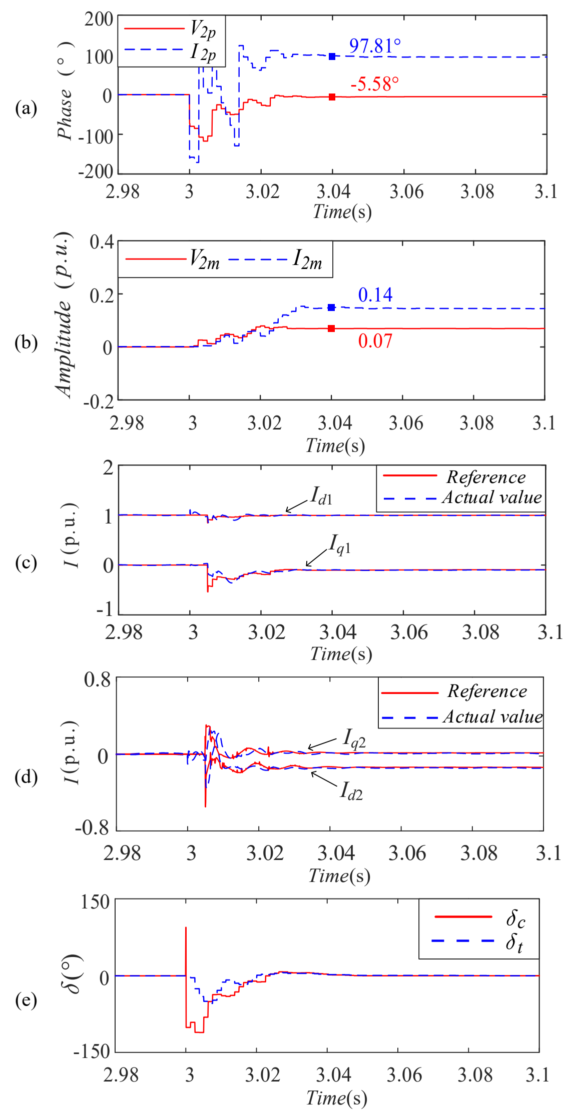

(f)
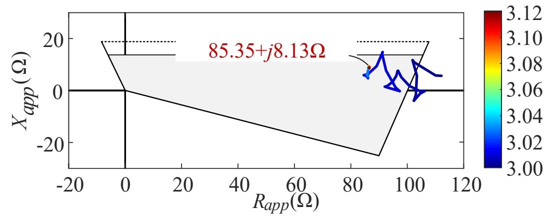

Fig. 20 Performance under an internal BCG fault. (a) Phase of negative-sequence voltage and current, (b) Amplitude of negative-sequence voltage and current, (c) Positive-sequence current (dq component), (d) Negative-sequence current (dq component), (e) Phase difference δ, (f) Measured Z_{app}.

Furthermore, Fig. 20 (c) and (d) show that the positive and negative-sequence currents can well track their respective references. Thus, the APC method can comply with the grid codes' negative-current injection requirement. Meanwhile, as shown in Fig. 20 (c), the APC method is also able to inject a considerable reactive current to meet the grid codes' reactive power generation requirement. Moreover, Fig. 20 (e) shows that the actual phase difference δ_t can be eliminated to around 0 within 30ms. And the measured Z_{app} in Fig. 20 (f) can rapidly converge to the point (85.35+j8.13 Ω) with an error of 0.28Ω (4% error rate) in the reactance part.

In summary, even under the strict German grid code, the proposed APC method is still effective, meeting the requirements of the grid code and locating the fault accurately.

E. Effectiveness Under IEEE 14-Bus System

To verify the effectiveness of the proposed APC method under a larger interconnected system, a modified 35kV, 50Hz IEEE 14-bus system with integration of a PV plant is built, as shown in Fig. 21. Where the detailed data of the 14-bus system is from [34]. The PV plant is connected to bus 8 through transmission line 1. The parameters of the PV plant and the protected line 1 are the same as the parameters in Table 3. Thus, the basic parameters of the M-side relay in Table 4 can be utilized. To determine the calculation formulas of the phase difference, the IEEE 14-bus system can be regarded as a local grid. Thus, the calculation formulas of the phase difference can be obtained by setting $Z^{II}_{L1,2}$ or $Z^{III}_{L1,2}$ in Table 2 to be 0.

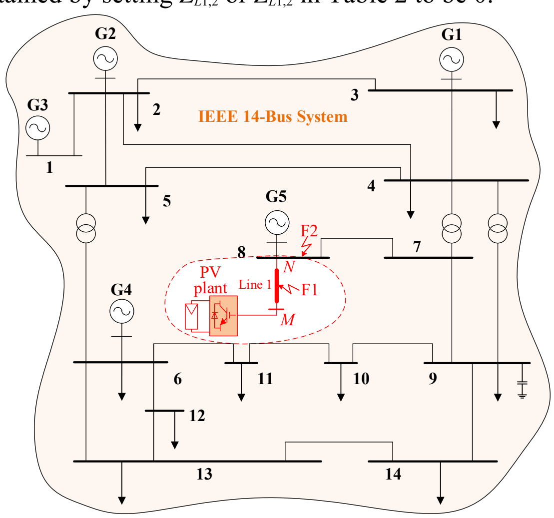

Fig. 21 PV plant integrated IEEE 14-bus system.

At 3.0s, two BCG faults with 20Ω fault resistance are respectively applied at F1 (at the midpoint of line 1) and F2 (at bus 8). The simulation results are shown in Fig. 22 and Fig. 23, respectively. It can be seen from Fig. 22 that the actual phase difference δ_t is rapidly eliminated by adjusting the calculated phase difference δ_c to 0. Correspondingly, the measured impedance Z_{app} converges to point (53.08+j8.06Ω). Compared to the actual fault reactance of 7.85Ω, the measurement error is only 0.21Ω (2.7% error).

In Fig. 23, the actual phase difference δ_t is also eliminated quickly. And the measured impedance Z_{app} is 55.42+j14.97Ω. Compared to the actual reactance of 15.69Ω, the measurement error is 0.72Ω (4.6% error). Hence, the F2 fault can be distinguished as a zone 2 fault correctly.

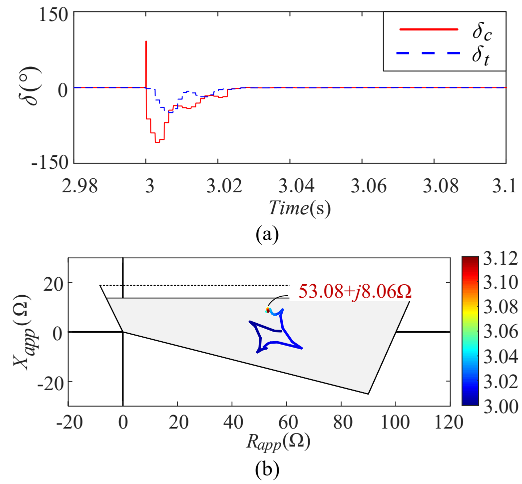

Fig. 22 Simulation results under F1 fault. (a) Phase difference δ, (b) Measured Z_{app}.

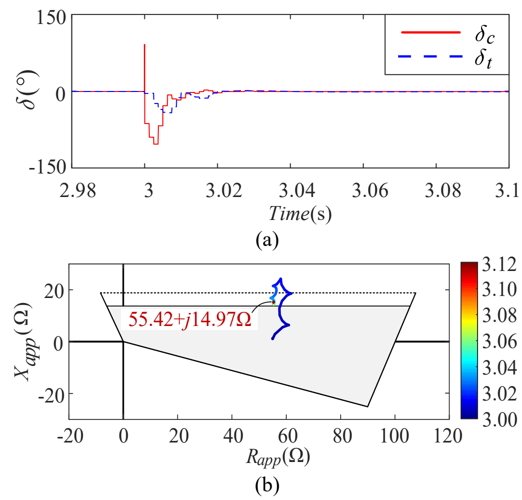

Fig. 23 Simulation results under F2 fault. (a) Phase difference δ, (b) Measured Z_{app}.

V. Conclusion

In this paper, an active phase control is proposed for the interfaced converter to address the reliability issues of distance relay in the renewable energy system. Benefiting from the accurate calculation of the phase difference, the proposed APC method can eliminate the phase difference within 25ms by regulating the converter current. Under internal faults, the distance relay can precisely measure fault reactance with the fault resistance up to 100Ω, and the maximum error rate is less than 5%. Under external faults, the proposed method can still ensure the correct operation of the distance relay.

In addition, under the grid codes with the requirements of reactive power generation and negative-sequence current injection, the proposed method is still effective. Moreover, the proposed protection scheme does not require modification of well-established distance relays, which can be directly applied to the interfaced converters of renewable sources.

VI. References

[1] B. Kroposki. et al., "Achieving a 100% Renewable Grid: Operating Electric Power Systems with Extremely High Levels of Variable Renewable Energy," *IEEE Power and Energy Mag.*, vol. 15, no. 2, pp. 61-73, Mar. 2017.

[2] A. S. Brouwer, et al., "Operational flexibility and economics of power plants in future low-carbon power systems," *Appl. Energy*, vol. 156, pp. 107-128, 2015.

[3] W. T. El-Sayed, E. F. El-Saadany and H. H. Zeineldin, "Interharmonic Differential Relay with a Soft Current Limiter for the Protection of Inverter-Based Islanded Microgrids," *IEEE Trans. Power Del*., early access, to be published.

[4] K. Jia, C. Gu, Z. Xuan, et al, "Fault Characteristics Analysis and Line Protection Design Within a Large-Scale Photovoltaic Power Plant," *IEEE Trans. Smart Grid*, vol. 9, no. 5, pp. 4099-4108, Sept. 2018.

[5] H. F. Habib, C. R. Lashway and O. A. Mohammed, "A Review of Communication Failure Impacts on Adaptive Microgrid Protection Schemes and the Use of Energy Storage as a Contingency," *IEEE Trans. Ind. Appl.*, vol. 54, no. 2, pp. 1194-1207, March-April 2018.

[6] D. S. Kumar, D. Srinivasan and T. Reindl, "A Fast and Scalable Protection Scheme for Distribution Networks With Distributed Generation," *IEEE Trans. Power Del*. vol. 31, no. 1, pp. 67-75, Feb. 2016.

[7] S. A. Saleh, "Signature-Coordinated Digital Multirelay Protection for Microgrid Systems," *IEEE Trans. Power Electron.*, vol. 29, no. 9, pp. 4614-4623, Sept. 2014.

[8] A. Hooshyar and R. Iravani, "Microgrid Protection," *Proceedings of the IEEE*, vol. 105, no. 7, pp. 1332-1353, July 2017.

[9] A. Sinclair, D. Finney, D. Martin, et al, "Distance protection in distribution systems: how it assists with integrating distributed resources," *IEEE Trans. Ind Appl.*, vol. 50, no. 3, pp. 2186–2196, May. 2014.

[10] Y. Liang, Y. Huo and F. Zhao, "An Accelerated Distance Protection of Transmission Lines Emanating from MMC-HVDC Stations," *IEEE J. Emerg. Sel. Top. Power Electron*., vol. 9, no. 6, pp. 7088-7098, Dec. 2021.

[11] K. E. Arroudi and G. Joos, "Performance of interconnection protection based on distance relaying for wind power distributed generation." *IEEE Trans. Power Del.*, vol. 33, no. 2, pp. 620–629, April 2018.

[12] A. Hooshyar, M. A. Azzouz and E. F. El-Saadany, "Distance Protection of Lines Emanating From Full-Scale Converter-Interfaced Renewable Energy Power Plants—Part I: Problem Statement," *IEEE Trans. Power Del*., vol. 30, no. 4, pp. 1770-1780, Aug. 2015.

[13] G. Ziegler, Numerical Distance Protection: Principles and Applications, 4th ed. Erlangen, Germany: Publicis Publishing, 2011, ch. 3.

[14] Y. Fang, K. Jia, Z. Yang, et al, "Impact of Inverter-Interfaced Renewable Energy Generators on Distance Protection and an Improved Scheme," *IEEE Trans. Ind. Electron.*, vol. 66, no. 9, pp. 7078-7088, Sept. 2019.

[15] Y. Liang, W. L. Li and Y. Huo, "Zone I Distance Relaying Scheme of Lines Connected to MMC-HVDC Stations During Asymmetrical Faults: Problems, Challenges and Solutions," *IEEE Trans. Power Del*., early access, to be published.

[16] S. Paladhi and A. K. Pradhan, "Adaptive Distance Protection for Lines Connecting Converter-Interfaced Renewable Plants," *IEEE J. Emerg. Sel. Top. Power Electron.*, early access, to be published.

[17] P. Mishra, A. K. Pradhan and P. Bajpai, "Adaptive Distance Relaying for Distribution Lines Connecting Inverter-Interfaced Solar PV Plant," *IEEE Trans. Ind. Electron.*, vol. 68, no. 3, pp. 2300-2309, March 2021.

[18] A. Banaiemoqadam, A. Hooshyar and M. A. Azzouz, "A Control-Based Solution for Distance Protection of Lines Connected to Converter-Interfaced Sources During Asymmetrical Faults," *IEEE Trans. Power Del.*, vol. 35, no. 3, pp. 1455-1466, June 2020.

[19] A. K. Pradhan and G. Joos, "Adaptive distance relay setting for lines connecting wind farms," *IEEE Trans. Energy Conv.*, vol. 22, no. 1, pp. 206–213, March 2007.

[20] G. Ziegler, Numerical Distance Protection: Principles and Applicant, 4th ed. Erlangen, Germany: Publicis Publishing, 2011.

[21] Z. Chu and F. Teng, "Short Circuit Current Constrained UC in High IBG-Penetrated Power Systems," *IEEE Trans. Power Syst.*, vol. 36, no. 4, pp. 3776-3785, July 2021.

[22] X. Liu, Z. Xu, G. Wang, et al., "Accurate estimation on AC short-circuit current for grid-connected MMC-HVDC system considering FRT and various control modes," *Int. J. Electr. Power Energy Syst.*, vol. 136, pp. 1-10, March 2022.

[23] S. Fariborz Zarei, M. A. Ghasemi, S. Khankalantary, "Current limiting strategy for grid-connected inverters under asymmetrical short circuit faults," *Int. J. Electr. Power Energy Syst.*, vol. 131, April 2021.

[24] P. Piya, M. Ebrahimi, M. Karimi-Ghartemani, et al, "Fault Ride-Through Capability of Voltage-Controlled Inverters," *IEEE Trans. Ind. Electron.*, vol. 65, no. 10, pp. 7933-7943, Oct. 2018.

[25] K. Jia, C. Gu, Z. Xuan, et al, "Fault Characteristics Analysis and Line Protection Design Within a Large-Scale Photovoltaic Power Plant," *IEEE Trans. Smart Grid.*, vol. 9, no. 5, pp. 4099-4108, Sept. 2018.

[26] Technical requirements for the connection and operation of customer installations to the high voltage network (TAR high voltage), Anwendungsregel, VDE-AR-N 4120: 2018-11, Germany, 2018.

[27] A. Haddadi, I. Kocar, J. Mahseredjian, et al, "Negative sequence quantities-based protection under inverter-based resources Challenges and impact of the German grid code," *Electric Power Systems Research*, vol. 188, July 2020.

[28] A. Haddadi, M. Zhao, I. Kocar, et al, "Impact of Inverter-Based Resources on Negative Sequence Quantities-Based Protection Elements," *IEEE Trans. Power Del.*, vol. 36, no. 1, pp. 289-298, Feb. 2021.

[29] M. Berger, I. Kocar, E. Farantatos and A. Haddadi, "Dual Control Strategy for Grid-Tied Battery Energy Storage Systems to Comply with Emerging Grid Codes and Fault Ride Through Requirements," *Journal of Modern Power Systems and Clean Energy*, early access, to be published.

[30] Technical manual for line distance protection REL650 (version 1.1 IEC), ABB, May 2020.

[31] DL/T584-2017, "Setting duide for 3kV~110kV power system protection e quipment", 2017.

[32] J. J. Q. Yu, Y. Hou, A. Y. S. Lam and V. O. K. Li, "Intelligent Fault Detection Scheme for Microgrids With Wavelet-Based Deep Neural Networks," *IEEE Trans. Smart Grid.*, vol. 10, no. 2, pp. 1694-1703, March 2019.

[33] M. S. Sachdev, R. Das, T. S. Sidhu, et al., "Understanding microprocessor -based technology applied to relaying," *IEEE Power System Relaying Com mittee*, Jan. 2009.

[34] Illinois Center for a Smarter Electric Grid. (2013). [Online]. Available FT P: http://publish. illinois.edu/smartergrid/